RSC Advances

PAPER

View Article Online
View Journal | View Issue

Cite this: *RSC Adv.*, 2016, **6**, 13554

Cancer theranosis using mono-disperse, mesoporous gold nanoparticles obtained *via* a robust, high-yield synthetic methodology†

Taeksu Lee,[a] Doyeon Bang,[a] Yong Wook Chang,[b] Yuna Choi,[c] Kwang Yeol Park,[c] Aram Oh,[d] Seungmin Han,[a] Sun Hee Kim,[e] Kwangyeol Lee,[d] Jin-Suck Suh,[c] Yong-Min Huh*[c] and Seungjoo Haam*[a]

Porous noble metal nanoparticles exhibit many attractive nanoplasmonic features, and these structures have potential applications in many fields. However, such applications have been hindered by a lack of synthetic methods with the ability to mass-produce mono-disperse nanoparticles. Current synthetic approaches to porous gold nanostructure fabrication involve galvanic replacement approaches or electrochemical deposition methods that are generally limited by stringent multi-step protocols and relatively low yields. Here, we introduce the facile synthesis of scalable, mono-disperse, mesoporous gold nanoparticles (MPGNs) using an acidic emulsification method. This method facilitates high synthetic yields (>93%) and tunable particle sizes (130–400 nm). MPGNs exhibit enhanced payloads of gadolinium (Gd), a contrast agent for magnetic resonance imaging. Additionally, they permit photo-thermal conversion under near-infrared light (NIR) irradiation due to the increased surface area to volume ratio and the unique, structure-mediated LSPR effect. Specifically, MPGNs fabricated using our method provided Gd payloads 2–4 orders of magnitude greater than previously reported theranostic nano-probes. We believe that our novel synthetic technique will not only contribute to large-scale production of homogeneous porous gold nanoparticles, but will also promote further research in porous noble metal nanostructures.

Received 23rd November 2015
Accepted 20th January 2016

DOI: 10.1039/c5ra24772a

www.rsc.org/advances

1. Introduction

Porous plasmonic nanomaterials have been studied extensively for potential technological applications in surface-enhanced Raman spectroscopy (SERS), drug delivery and therapeutics, catalysis, and non-linear optics.[1–5] Because their plasmonic resonance responses and local field enhancement depend on accurately controlling nanoparticle size and shape (but still require mass production for widespread applications), the primary challenge associated with development of these porous nanostructures is achieving high yield with sharp mono-dispersity.

Currently, the most successful methods for obtaining mono-dispersed, shape-regulated plasmonic nanomaterials employ oxidative etching or seed-mediated growth of gold nanoparticles (*i.e.* mono-disperse gold nano-triangles,[6,7] gold nano-bipyramids[8] and gold nano-dumbbells[9]). However, these processes require an additional size-sorting step to remove byproducts, such as seed particles with certain surfactant, and eventually result in low synthetic yields.

Aside from those mentioned above, self-assembly, template, electrochemical and galvanic replacement methods have been introduced to obtain nanoporous gold structures. These approaches succeeded in increasing the surface area to volume ratio of the noble metal nanostructures, ultimately increasing the number of catalytic sites and boosting loading capacity. However, harsh reaction conditions, the necessity of temperatures greater than 80 °C,[1,5,10–12] multiple synthetic steps and the need for a silver sacrificial template resulted in the formation of poly-disperse porous nanoparticles and low synthetic yields, hindering the practical application of such methods.[3,5,13–15]

In this report, we introduce an acidic nano-emulsification method for mono-disperse porous gold nanoparticle (MPGN) fabrication with highly improved production yield (>93%) (Scheme 1a). We dissolved aniline monomers (as an oxidant) in an acidic solution and gold precursors ($HAuCl_4$) were added. A

[a]*Department of Chemical and Biomolecular Engineering, Yonsei University, Shinchon-dong, Seodaemun-gu, Seoul 120-749, Republic of Korea. E-mail: haam@yonsei.ac.kr*

[b]*Department of Materials Science and Engineering, Yonsei University, Shinchon-dong, Seodaemun-gu, Seoul 120-749, Republic of Korea*

[c]*Department of Radiology, Yonsei University, Seoul 120-752, Republic of Korea. E-mail: ymhuh@yuhs.ac*

[d]*Department of Chemistry, Korea University, Seoul 136-701, Republic of Korea*

[e]*Korea Basic Science Institute (KBSI) Seoul, Republic of Korea*

† Electronic supplementary information (ESI) available. See DOI: 10.1039/c5ra24772a

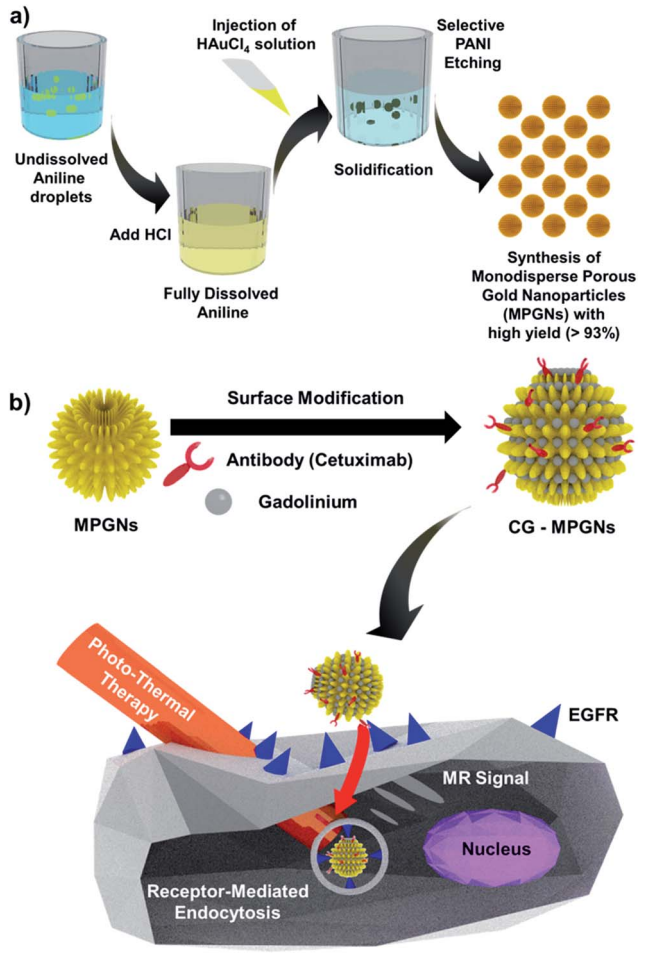

Scheme 1 (a) Schematic illustration of synthetic procedure for MPGNs. Aniline monomers were fully dissolved in the acidic solution and the polyaniline and gold composite nanoparticles are first synthesized *via* the mutual redox reaction. Monodisperse and mesoporous gold nanoparticles with high yield (>93%) were obtained after the selective removal of polyaniline with *n*-methylpyrrolidone. (b) Surface modification of MPGNs with gadolinium (Gd) and therapeutic antibody (cetuximab) for the simultaneous diagnosis by MR imaging and photo-thermal ablation of epithelial cancer cells.

mutual redox process between $HAuCl_4$ and aniline was performed to fabricate the MPGNs. This process not only resulted in completely-solubilized aniline and facilitated the redox reaction for increasing production yield, but also hindered the generation of oligomers and excessive branching of polyaniline (PANI).[16–18] After selective etching of PANI with *n*-methyl pyrrolidone, MPGNs revealed sharp mono-dispersity, without the need for a size-sorting step, and MPGN fabrication could be completed in 20 min with a high Au yield (much faster than previously reported processes).[3,5–7,9,19] Moreover, MPGN dimensions could be controlled (between 130 and 400 nm) by varying experimental conditions.

Finally, to investigate potential applications of MPGNs as theranostic cancer probes, we chelated gadolinium (Gd; a contrast agent for magnetic resonance imaging) by conjugating diethylenetriaminepentaacetic acid (DTPA) to the MPGNs (Scheme 1b). We found that MPGNs delivered 2×10^3-fold higher Gd payloads compared to spherical gold nanoparticles with similarly sized MPGNs, due to their enlarged surface areas. Furthermore, MPGN Gd payloads were approximately two to four orders larger than those of previously introduced theranostic nanoprobes (polymer nanoparticles, mesoporous silica nanoparticles, other gold based nanostructures and so on).[20–23] MPGN surfaces were further modified with a therapeutic antibody, cetuximab (CET), in order to target epidermal growth factor receptor (EGFR) abundant cancer cells.[20,24,25] The effective photo-thermal conversion of MPGNs based on selective absorption of near-infrared (NIR) light revealed light efficacy for treatment of cancer cells. The sharp mono-dispersity of MPGNs resulted in uniform Gd payloads and photo-thermal conversion efficacy, which may ultimately contribute to accurate diagnosis and treatment of specific types of cancer.

2. Materials and methods

2.1. Materials

Aniline, gold(III) chloride trihydrate, diethylenetriaminepentaacetic dianhydride (DTPA-DA) and gadolinium(III) chloride hexahydrate ($GdCl_3 \cdot 6H_2O$) were obtained from Sigma Aldrich. *N*-Methyl-2-pyrrolidone (NMP) was purchased from Duksan Pure Chemicals Co. and 1-ethyl-3-(3-dimethylaminopropyl)-carbodiimide (EDC) was obtained from Tokyo Chemical Industry (TCI). Carboxy-PEG-thiol compound and sulfo-*N*-hydroxysuccinimide (sulfo-NHS) were purchased from Pierce (Thermo Scientific, Waltham, MA, USA). Chemical reagents were not subjected to further purification. Cetuximab (CET) was obtained from Roche Pharmaceutical, Ltd. Dulbecco's phosphate-buffered saline (PBS, pH 7.4) was purchased from Hyclone. Dulbecco's modified Eagle's medium (DMEM) and fetal bovine serum (FBS) were purchased from Gibco. A-431 and MCF-7 cells were obtained from the American Type Culture Collection (ATCC). Prior to use, all glassware was cleaned with a piranha solution of concentrated sulfuric acid (98%) and hydrogen peroxide (30%). All solutions were prepared using Millipore deionized water (DW) with a resistivity lower than 18.2 MΩ cm at 25 °C (Vivendi Water Systems).

2.2. Synthesis and characterization of mono-disperse, mesoporous gold-nanoparticles (MPGNs)

In order to synthesize MPGNs with ultra-high yield, MPGNs were fabricated *via* a surfactant-free emulsion method in an acidic aqueous solution. In short, aniline monomers (0.1 M) were dissolved in an aqueous preparation of hydrochloric acid (pH 1, 20 mL). The metastable aniline emulsion was solidified *via* injection of an aqueous $HAuCl_4$ solution (1 mL, 0.1 M) under emulsification for 20 min with an ultra-sonicator. The relative power of the sonicator was varied to control MPGN size. Upon reaction completion, the synthesized nanoparticles were purified with a 1 M NaOH solution. The MPGNs were subjected to three cycles of centrifugation with 1-methylpyrrolidone (NMP). The final product was re-dispersed in DW. For the scale up, 2

mL of 0.1 M $HAuCl_4$ solution were added to the HCl solution (40 mL, 0.1 M of aniline). The remainder of the procedure was identical to that described above.

MPGN size distributions were analyzed using laser scattering (ELS-Z, Otsuka Electronics), and synthetic yields were characterized using an inductively-coupled plasma optical emission spectrometer (ICP-OES, Perkin Elmer). Morphology of prepared nanoparticles was investigated *via* scanning electron microscopy (SEM, JEOL JSM-7800F, Japan), transmission electron microscopy (TEM, JEM-1011, JEOL, Japan) and high-resolution TEM (JEM-ARM 200F, JEOL at 200 kV and TECNAI G2 20 S-Twin operated at 200 kV). In order to measure MPGN surface area and pore-size distribution, nitrogen adsorption and desorption isotherms at 77 K were measured using a Surface Area & Pore Size Analyzer (BET, QuadraSorb SI, Quantachrome Instrument, USA). Prior to BET measurement, samples were pre-treated in a nitrogenous environment for 12 h at 300 K. Pore-size distributions were calculated from desorption branches of isotherms using the Barrett–Joyner–Halenda (BJH) method.

2.3. MPGN surface modification

MPGN surfaces were first modified with amine groups by dispersing 1 mg of MPGNs in 1 mL of a 1×10^{-2} M cysteamine solution for 6 h under magnetic stirring.[26] Then, excess DTPA-DA was covalently conjugated to the surface of MPGNs *via* EDC/NHS chemistry at 85 °C for 2 h. The purified DTPA-conjugated MPGNs were collected *via* centrifugation. For pegylation, 3 mg carboxy-PEG-thiol was mixed with 1 mg of DTPA-conjugated MPGNs for 24 h at room temperature. The mixture was centrifuged to remove unbound PEG molecules. To conjugate CET to the surface of MPGNs, EDC (8.82×10^{-2} mmol), sulfo-NHS (8.82×10^{-2} mmol), and 200 μL of CET (5 mg mL^{-1}) were added to 10 mL of MPNGs (1 mg mL^{-1}). The mixture was reacted at 4 °C for 6 hours. 10 mg of $GdCl_3 \cdot 6H_2O$ were then reacted with 1 mg of CET-conjugated MPGNs (CG-MPGNs). The product was purified by dialysis against PBS.

CG-MPGN size distributions were analyzed using laser scattering (ELS-Z, Otsuka Electronics). Additionally, CG-MPGN stability at various serum concentrations (FBS 0, 10, 20, 30, 40 and 50%) was analyzed using laser scattering. The residual weight (%) of MPGNs in DMGNs was analyzed using a thermogravimetric analyzer (SDT-Q600, TA instrument). Absorbance of CG-MPGNs was measured with a UV-Vis spectrophotometer (Optizen 2120UV MECASYS Co). To evaluate the photothermal effects of CMGNs upon NIR laser irradiation, CG-MPGNs (0.5 mg mL^{-1}) were exposed to NIR coherent diode laser light (808 nm, 15 W cm^{-2}) for 7 min. Increase in solution temperature was monitored using a thermocouple-based multimeter probe (187 True RMS Multi-meter, Fluke). The amount of Gd loaded in CG-MPGNs was analyzed using an ICP-OES.

2.4. Preparation of smooth gold nanoparticles (sGNPs)

We prepared smooth gold nanoparticles (sGNPs) using hydroquinone as a reducing agent.[27] First, 12 nm gold nanoparticle seed solutions were prepared *via* sodium citrate reduction. Five milliliters of 1% sodium citrate solution (by weight) were added to 100 mL of ultra-pure distilled water and magnetically stirred at 95 °C. Upon solution boiling, 1 mL of 1% (w/v) $HAuCl_4$ solution was injected. We purified the products with centrifugal filters (Centriprep YM-3, 10 kDa molecular weight cutoff (MWCO), Amicon, Millipore Corporation, Billerica, MA, USA) in triplicate at 4000 rpm for 10 min. For synthesis of sGNPs, 100 μL of a 1% (w/v) $HAuCl_3$ solution was added to 9.8 mL of deionized water in a 20 mL vial at room temperature. Then, 32 μL of seed solution were added. Twenty-two microliters of a 1% sodium citrate solution were added, immediately followed by addition of 100 μL of 0.03 M hydroquinone. Surface modification with DTPA was the same as that of the MPGNs.

2.5. ENDOR spectroscopy measurements

All pulsed EPR data were collected at Western Seoul Center, KBSI. Thirty-four GHz-pulsed EPR data were obtained on a Bruker ELEXSYS 580 spectrometer using an EN5107D2 resonator. Cryogenic temperatures were achieved with an Oxford CF-935 cryostat and Oxford ITC temperature controller. All measurements were performed at 8 K. Mims ENDOR was carried out using the p/2-*t*-p/2-*T*-p/2-*t*-echo pulse sequence, with microwave pulse lengths of 32 ns (p/2 pulse) and an inter-pulse time of $t = 200$ ns. RF was applied at time T (20 ms) to drive nuclear spin transitions. All ENDOR measurements were acquired using stochastic sampling to avoid baseline drift, ensuring more accurate quantitative analysis. Electron spin echo-detected field sweep experiments were performed using the same three pulse sequences as used for the Mims experiments.

2.6. Cell culture and cellular experiments with CG-MPGNs

Cytotoxic effects of CG-MPGNs against A-431 and MCF-7 cells were analyzed using colorimetric assay based on mitochondrial oxidation of 3-(4,5-dimethylthiazolyl-2)-2,5-diphenyltetrazolium bromide (MTT). A-431 (EGFR+) and MCF-7 (EGFR−) cells were maintained in DMEM containing 10% fetal bovine serum (FBS) and 1% antibiotics at 37 °C in a 5% CO_2 atmosphere. Cells were diluted to a density of 1.0×10^4 cells/100 μL in a 96-well plate and incubated at 37 °C in a 5% CO_2 atmosphere. Cells were treated with various concentrations of CG-MPGNs (5×10^{-11} to 5×10^{-1} mg mL^{-1}) for 4 h and rinsed with 100 μL PBS (pH 7.4, 1 mM). Freshly-prepared MTT solution was then added. Cells were incubated for 4 h, and 100 μL of solubilization solution (10% sodium dodecyl sulfate in 0.01 M HCl) were added. After overnight incubation, the absorbance of each well was measured using an ELISA plate reader (Spectra MAX 340, Molecular Devices) at an absorbance wavelength of 575 nm and a reference wavelength of 650 nm.

The cellular targeting efficiency of CG-MPGNs was measured using MR imaging of A-431 and MCF-7 cells. A-431 and MCF-7 cells (1×10^7 cells from each line) were incubated with CG-MPGNs (0.5 mg mL^{-1} and 0.1 mg mL^{-1}, respectively). After incubation for 6 h, cells were washed in triplicate with PBS. Next, both cell lines were harvested and 200 μL of 4% paraformaldehyde were added to re-suspend the cells. The cellular

internalization of CG-MPGNs was also confirmed by TEM (JEOL-1100).

In order to test photo-thermal efficiency of CG-MPGNs, A-431 and MCF-7 cells (5×10^5 cells per well) were incubated with 1 mL of CG-MPGNs (0.5 mg mL^{-1} in DMEM) at 37 °C in a 5% CO_2 atmosphere. After 2 h, cells were washed with PBS, and 2 mL of DMEM with 10% FBS were added to each well. An NIR coherent diode laser (808 nm, 25 W cm^{-2}, UM30K, Jenoptik) was used to irradiate each well for 10 min, and cells were washed with PBS. Distribution of live cells was detected using an optical system microscope (Olympus BX51) after staining with calcein AM and ethidium homodimer-1 (EthD-1).

2.7. MR imaging procedure

We performed solution and *in vitro* MRI experiments with a 1.5 T clinical MRI instrument with a micro-47 surface coil (Intera; Philips Medical Systems, Best, The Netherlands). T_1 weights of the CG-MPGN solution and the CG-MPGN treated cells (A-431 and MCF-7 cells) were measured at room temperature with the following MR parameters: 540 × 540 μm, section thickness = 3.0 mm, TE = 14 ms, TR = 6.6 ms, and number of acquisitions = 1. The relaxivity coefficient (mm^{-1} s^{-1}) was equal to the ratio of $r_1(1/T_1$ [s^{-1}]) to Gd concentration.

3. Results and discussion

In order to obtain MPGNs, we fully dissolved aniline ($C_6H_5NH_2$) monomers in acidic solutions (pH 1) to form anilinium molecules ($C_6H_5NH_3^+$), and produced polyaniline (PANI)/Au hybrid nanoparticles *via* the nano-emulsification method described. The mutual redox reaction of $HAuCl_4$ to Au^0 ($Au^{3+} \rightarrow Au^0$) and anilinium ion to PANI ($C_6H_5NH_3^+ \rightarrow ([C_6H_4NH]_2[C_6H_4N]_2)_n$) was successful, and the selective de-alloy process was followed with *n*-methylpyrrolidone (NMP) to remove PANI.

After the reaction, we confirmed that MPGNs enhanced Au production yield (93.3 ± 1.3%, detected using an ICP-OES) and mono-dispersity (Fig. 1a and b). On the contrary, porous gold nanoparticles synthesized in neutral aqueous solution exhibited lower synthetic yields (37.3 ± 3.1%) and wider size distributions (Fig. S1†). It should be noted that no size selection or further purification processes were applied.[6,7,9] This highly improved MPGN yield and mono-dispersity may be the outcome of the acidic conditions of the redox process. First, protons increased the solubility of aniline, which was beneficial for promoting interaction between gold and anilinium ions. However, in neutral conditions, aniline formed unstable droplets in the aqueous phase, and aniline molecules inside the droplets rarely interacted with gold ions (potentially resulting in diminished MPGN yield). In the case of PANI polymerization in neutral conditions, both oligomers and polymers are synthesized, and excessive PANI branching is resulted. However, under low pH conditions, non-branched emeraldine is primarily polymerized.[16–18] Since PANI acted as a synthetic template for MPGNs, PANI byproducts in neutral conditions engender a heterogeneous morphology, whereas uniform MPGNs are generated in acidic solutions.

The crystalline structures of individual NPG structures were analyzed using high-resolution TEM (HR-TEM) (Fig. 1c and d), corresponding fast Fourier transform (FFT) patterns (Fig. 1e) and X-ray diffraction (XRD) (Fig. 1f). Fig. 1d demonstrates clear lattice fringes at the periphery of the nanoparticles. The spacing between lattice fringes were analyzed as 0.234 nm and 0.203 nm, corresponding to the (111) and (200) facets of MPGNs. The FFT pattern in Fig. 1e presented a diffraction pattern of MPGNs with corresponded lattice parameters. These figures were also well matched with the XRD data (Fig. 1f), indicating that MPGNs were pure, face-centered cubic gold structures.[9] Nitrogen absorption measurements clearly demonstrated uniform mesopores formed in NPG, and the specific surface area was as high as 27.3 m^2 g^{-1}. It was analyzed from the linear part of the BET plot (Fig. 1g). Additionally, the average pore size was 3.9 nm. Fig. 1h exhibits a sharp peak centered at a value of 3.3–4.4 nm, implying a narrow mesopore size distribution. 30 days after synthesis, we performed light scattering and TEM analysis and revealed the MPGNs were also highly stable without showing size and morphological variance (Fig. S2†).

MPGN sizes were systematically controlled by adjusting the relative power (W) of the sonicator. It is worth noting that the concentrations of aniline, Au^{3+} and protons were held constant in all experiments. With sonicator powers of 300 W, 190 W and 150 W, average MPGN sizes were 131.0 ± 2.7 nm (Fig. 2a), 309.6 ± 7.7 nm (Fig. 2b) and 391.9 ± 12.0 nm (Fig. 2c), respectively. These values were consistent with the light scattering data (Fig. 2d). Synthetic yield of MPGNs was over 90% under all reaction conditions, and mono-dispersity was preserved. As shown in Fig. 2e, the size increment of MPGNs resulted in high absorption in the NIR region. This is likely because the optical properties of gold nanostructures are very sensitive to physical dimensions, and the absorbance spectra were altered by the MPGN diameter.

MPGN synthesis using acidic emulsion methods could be readily scaled up by increasing the quantity of aniline and metal precursors. For example, we doubled the amount of all reactants and compared yields and MPGN morphologies. Irrespective of the experiment scale, MPGN production yield was higher than 93%, and uniform MPGNs (130 nm) were fabricated (Fig. S4†). Given the ease of operation of our method, over 1 kg of monodisperse and mesoporous gold nanoparticles were expected as a result of enlarging the number of reactors. This demonstrates that acidic emulsion techniques for MPGN synthesis are capable of mass production of uniform, porous metal nanomaterials with superb yield. Judging by these results, our acidic nano-emulsification method is a robust route for generating porous noble metal nanoparticles.

The highly porous structure and distinct LSPR response in the NIR region of MPGNs allowed us to study their theranostic performance. Since MPGNs with diameters greater than 300 nm are inappropriate for bio-medical applications,[15,24] MPGNs with diameters of approximately 130 nm were chosen for the following experiments. We began by loading Gd, the contrast agent of MRI, on the surface of MPGNs. Gd was chosen because MRI is a highly reliable technique for detecting cancer, based on its non-invasiveness and tomographic real-time imaging.[24,28]

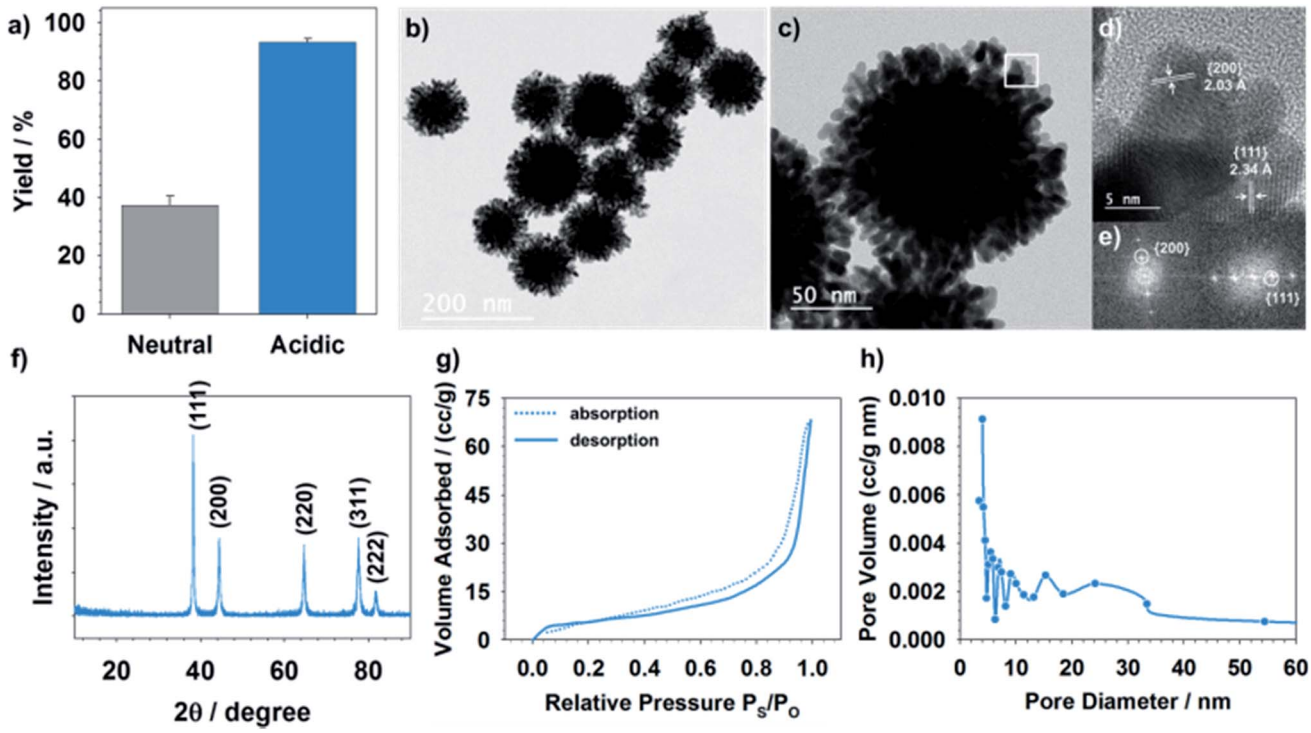

Fig. 1 (a) MPGN yields after reaction under neutral and acidic conditions. Yields were detected using an inductively-coupled plasma optical emission spectrometer (ICP-OES). (b) Representative transmission electron microscopy (TEM) images of MPGNs. (c) High-resolution TEM (HR-TEM) images of MPGNs. (d) Magnified images showing lattice fringes, denoted by areas marked with a white box at the periphery of the particle. (e) FFT pattern of MPGNs. (f) X-ray diffraction (XRD) pattern of MPGNs with inserted main crystalline phases of MPGNs. (g) N_2 adsorption–desorption isotherms and (h) corresponding MPGN pore size distributions.

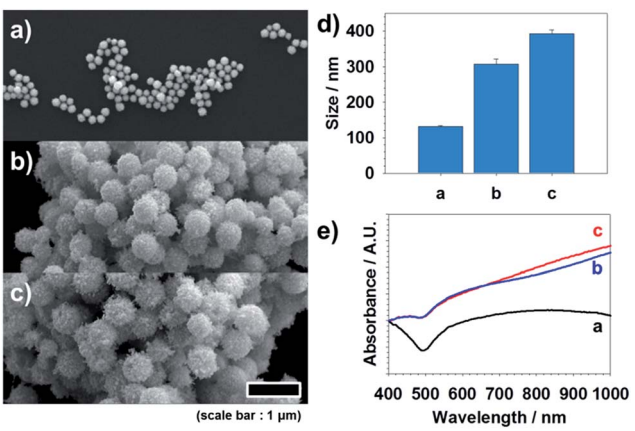

Fig. 2 SEM images of MPGNs with tunable dimensions. The average diameter of each sample was (a) 131.0 ± 2.7 nm; (b) 309.6 ± 7.72 nm; (c) 391.9 ± 12.0 nm. The scale bar represents 1 μm. (d) MPGN hydrodynamic diameters and (e) UV-Vis spectra (normalized at 400 nm) are depicted in a–c.

Additionally, Gd enhances MR signals without disrupting magnetic homogeneity.[20,29] First, we introduced diethylenetriaminepentaacetic acid (DTPA) to the MPGNs to chelate and reduce the potential toxicity of Gd.[30] By using cysteamine, MPGNs were covered with functional amine groups and diethylenetriaminepentaacetic dianhydride (DTPA-DA) molecules were conjugated to MPGNs by fabrication amide bonds. Carboxy-PEG-thiol was then added for increased colloidal stability of MPGNs, as well as antibody conjugation. CET, an anti-EGFR, was conjugated to target EGFR abundant cancer cells. Finally, Gd was chelated (CG-MPGNs). After surface modification, the colloidal size of CET-MPGNs increased (181.9 ± 7.8 nm, by light scattering) compared to bare MPGNs (131.0 ± 2.7 nm) (Fig. 3a). The Gd payload per 1 mg of gold at NPG, measured by ICP-OES, was 81.3 ± 2.1 mg, a result about 2×10^3 times higher than spherical gold nanoparticles with similarly sized MPGNs (Fig. S5† and 3b). We estimated that approximately 9.84×10^7 Gd molecules were associated with a single CG-MPGN particle. This value was approximately 2–4 orders of magnitude higher than previously reported for Gd loading agents such as polymer nanoparticles, mesoporous silica nanoparticles, lipoprotein nanocarriers and porous polymersomes.[20–23,31] The significant difference in Gd loading capacity was due to the highly porous structure and increased surface area of MPGNs.

We performed MRI experiments with CG-MPGNs to assess performance as an MR contrast agent (Fig. 3c and d). The relaxivity coefficient (r_1) of CG-MPGNs was calculated as the linear fit of five different Gd concentrations dissolved in DW at 1.5 T. The r_1 value was 14.5 ± 0.9 mM^{-1} s^{-1}, and the resultant r_1 value for each CG-MPGN particle was (1.43 ± 0.1) × 10^9 mM^{-1} s^{-1}. These values were significantly elevated compared to the clinical contrast agent, Doratem (4.0 mM^{-1} s^{-1}). Based on SBM

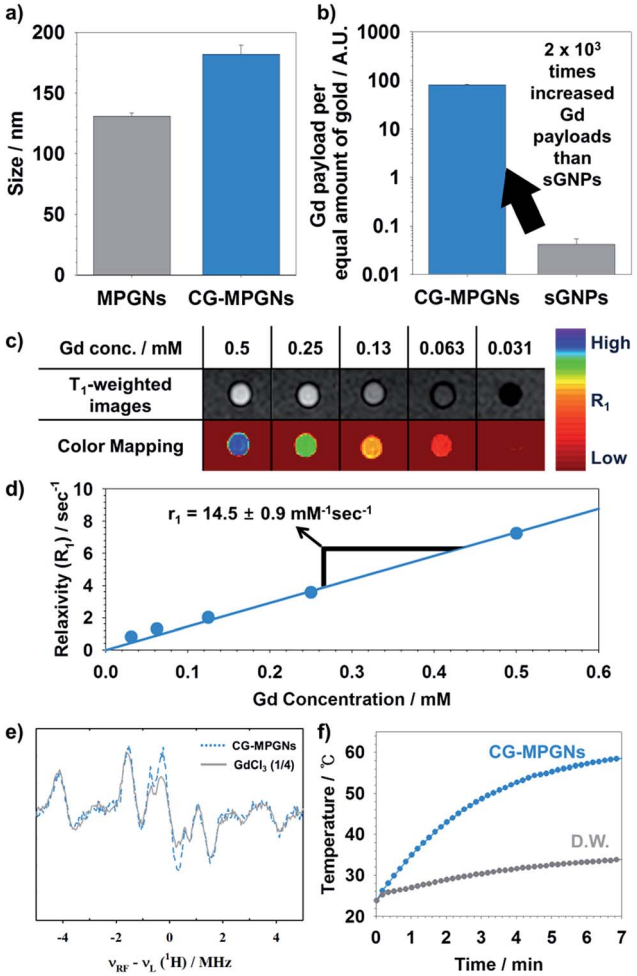

Fig. 3 (a) Hydrodynamic diameters of bare MPGNs before and after surface modification with CET, DTPA, PEG and Gd. (b) Relative amount of Gd payload per equal amount of gold between CET-MPGNs and smooth gold nanoparticles (sGNPs), characterized by ICP-OES. (c) Magnetic resonance (MR) images and (d) relaxivity (r_1) graph against CG-MPGN concentration (0–0.5 × 10^{-3} M Gd), measured at 25 °C with a 1.5 T MRI instrument. (e) First derivative of the spectra of normalized ^{1}H-Mims ENDOR spectra of $GdCl_3$ (scaled by a factor of 1/4) and CG-MPGNs. (f) Temperature increment profile for CG-MPGNs (blue line with circles) and DW (grey line with grey diamonds) with an NIR laser over a 7 min time period (wavelength = 808 nm, laser power = 15 W cm^{-2}). Real-time solution temperatures were monitored using a multimeter probe with a thermocouple (187 True RMS Multimeter, Fluke).

theory, the significant increase in r_1 was because the q value of Gd in CG-MPGNs increased to 2 (by normalized ^{1}H ENDOR spectra (Fig. 3e)), a value higher than that of commercial contrast agents ($q = 1$) and one that could facilitate the water exchange rate. In addition, the porous structure of CG-MPGNs facilitated the loading of 9.84 × 10^7 molecules of Gd per CG-MPGN for prolonged rotational correlation time (τ_R).[32–34]

The absorbance peak of CG-MPGNs was a broad absorption band observed at around 800 nm, which fell within the wavelength of the illuminated laser (808 nm). Therefore, the absorbed light energy was efficiently converted to heat upon NIR laser illumination (Fig. 3f). The temperature of a solution containing 0.5 mg mL^{-1} of CG-MPGNs increased instantly, and was saturated at temperatures above 59 °C after 7 min of illumination (laser power = 15 W cm^{-2}). However, the increase in solution temperature without CG-MPGNs (DW only) was nonsignificant. CG-MPGNs exhibited excellent colloidal stability without any aggregation or precipitation over a wide range of FBS concentration (0–50%) and pH (pH 4–10), because the cover layer of DTPA and PEG chains protected CG-MPGNs from attack by protein and proton concentration variances (Fig. S8†).

We next evaluated the *in vitro* theranostic efficiency of CG-MPGNs against target cancer cell lines (A-431: high EGFR expression, MCF-7: low EGFR expression). In advance, we performed MTT assays to examine the cytotoxicity of CG-MPGNs after treatment of cells with different CG-MPGNs concentrations (5 × 10^{-11} mg mL^{-1} to 0.5 mg mL^{-1}) for 4 h at 37 °C. No significant inhibition of growth or proliferation was detected at CG-MPGN concentrations up to 0.5 mg mL^{-1} in either of the two cell lines (Fig. S9†). Furthermore, cellular TEM images presented the A-431 cells internalized CG-MPGNs through the receptor mediated endocytosis (Fig. S10†). The CG-MPGNs treatment on cells did not induced cellular morphology variance. It was also found the CG-MPGNs conserved their morphologies and dimensions in the high-magnification images. On the contrary, we couldn't found CG-MPGNs on the MCF-7 cells in the TEM images. The engulfment of CG-MPGNs into the cellular region was important for versatile cancer theranosis.

The investigation of selective cancer diagnostic ability in CG-MPGNs was followed for A-431 and MCF-7 cell lines *via* MRI. T_1-weighted MR images of A-431 cells treated with CG-MPGNs resulted in a bright signal that became increasingly hyperintense with increasing nanoparticle concentration (Fig. 4a). In contrast, there was no significant difference in the intensity of CG-MPGN-treated MCF-7 cells and non-treated cells. Accordingly, the MR signal intensity ratio ($\Delta R_1/R_{1\text{Non-treatment}}$, where $\Delta R_1 = R_1 - R_{1\text{Non-treatment}}$) in A-431 cells (683.4 ± 23.1% at 0.5 mg mL^{-1} CG-MPGNs and 81.1 ± 7.4% at 0.1 mg mL^{-1} CG-MPGNs) was much higher than that of MCF-7 cells (54.7 ± 5.4% at 0.5 mg mL^{-1} CG-MPGNs and 9.2 ± 2.1% at 0.1 mg mL^{-1} CG-MPGNs) (Fig. S10†). These results were attributed to that CET on CG-MPGNs selectively diagnosed EGFR on A-431 cells and increment of both the r_1 value and the Gd payload in the CG-MPGNs.

We next performed synchronous photo-thermal therapy experiments by incubating A-431 and MCF-7 cells with 0.5 mg mL^{-1} CG-MPGNs for 2 h (Fig. 4b). Each cell line was irradiated with an NIR laser at 25 W cm^{-2} for 10 min and stained with both calcein AM to detect live cells (green fluorescence) and ethidium homodimer-1 (EthD-1) to detect dead cells (red fluorescence).[20] Due to CET and the unique, structure-mediated LSPR phenomena of CG-MPGNs, A-431 and MCF-7 cells treated with CG-MPGNs under photo-thermal therapy revealed a vivid red spot at the center of A-431 cell plates, likely because of cell death in response to NIR laser irradiation. Cells outside of the laser remained viable, but none of the control groups (non-treated A-431 and MCF-7 cells, CG-MPGNs treated MCF-7 cells) demonstrated noticeable cancer cell damage (Fig. S11†).

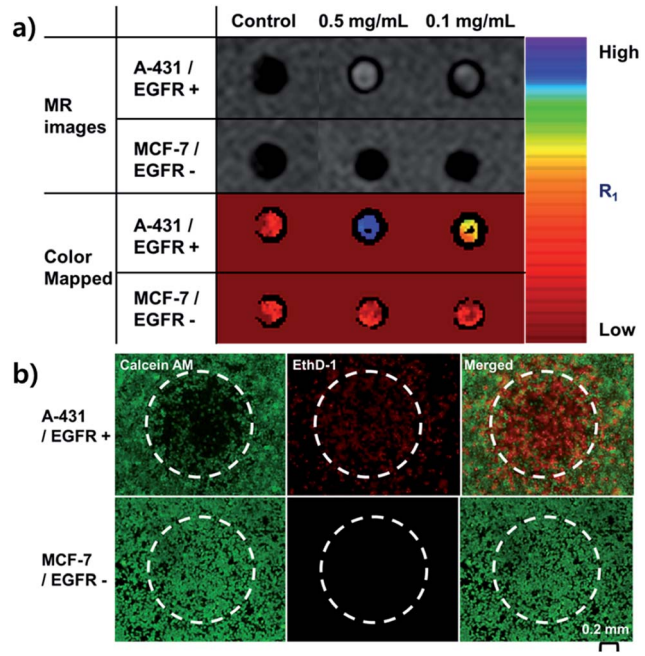

Fig. 4 (a) T_1-mapped and respective color-mapped MR images of A-431 (EGFR+) and MCF-7 (EGFR−) cell lines after treatment with various concentrations of CG-MPGNs (0.5 and 0.1 mg mL^{-1}). (b) Fluorescence microscopy images of A-431 and MCF-7 cells stained with calcein AM and ethidium homodimer-1 (EthD-1) after treatment with CG-MPGNs for 2 h followed by NIR laser irradiation for 10 min (808 nm, 25 W cm^{-2}). White-dotted curves represent the location of the laser beam. The scale bar represents 200 μm.

4. Conclusions

We have demonstrated an improved acidic emulsification technique for fabricating mono-disperse, mesoporous gold nanoparticles with a superb yield (>93%). Our method was rapid and simple, and enabled fabrication without size sorting or separation of byproducts. Full dissolution of aniline monomers in the acidic solution promotes the formation of MPGNs with high yield and mono-dispersity by increasing the probability of interaction with gold precursors and anilinium ions. Full dissolution of aniline also hinders the synthesis of oligomers and branched PANI, a byproduct resulting in poly-dispersity of MPGNs. The resultant MPGNs were able to deliver Gd loads 2–4 orders of magnitude higher than previously reported probes, and revealed photo-thermal efficiency. Finally, mean MPGN diameter was systematically controlled (between 130 and 400 nm) by varying experimental conditions. Our synthetic protocol is generic, and can be extended to various types of porous metal nanostructures by altering the metal precursors and reducing agents. Our method ultimately has applications in fields such as theranosis, surface-enhanced Raman scattering, nano-electrodes, fuel cells, and catalysis, among others.

Acknowledgements

This work was supported by the Center for BioNano Health-Guard funded by the Ministry of Science, ICT & Future Planning as Global Frontier Project (Grant Number H-GUARD_2013M3A6B2078946) and Bio & Medical Technology Development Program of the National Research Foundation (NRF) funded by the Ministry of Science, ICT & Future Planning (NRF-2015M3A9D7029834).

Notes and references

1 S. Pedireddy, H. K. Lee, W. W. Tjiu, I. Y. Phang, H. R. Tan, S. Q. Chua, C. Troadec and X. Y. Ling, *Nat. Commun.*, 2014, **5**, 4947.
2 H. du Toit and M. Di Lorenzo, *Sens. Actuators, B*, 2014, **192**, 725–729.
3 Z. Qi, U. Vainio, A. Kornowski, M. Ritter, H. Weller, H. J. Jin and J. Weissmuller, *Adv. Funct. Mater.*, 2015, **25**, 2530–2536.
4 X. Y. Lang, A. Hirata, T. Fujita and M. W. Chen, *Nat. Nanotechnol.*, 2011, **6**, 232–236.
5 H. Jang and D. H. Min, *ACS Nano*, 2015, **9**, 2696–2703.
6 L. Scarabelli, M. Coronado-Puchau, J. J. Giner-Casares, J. Langer and L. M. Liz-Marzan, *ACS Nano*, 2014, **8**, 5833–5842.
7 L. Chen, F. Ji, Y. Xu, L. He, Y. F. Mi, F. Bao, B. Q. Sun, X. H. Zhang and Q. Zhang, *Nano Lett.*, 2014, **14**, 7201–7206.
8 J. R. G. Navarro, F. Lerouge, G. Micouin, C. Cepraga, A. Favier, M. T. Charreyre, N. P. Blanchard, J. Lerme, F. Chaput, M. Focsan, K. Kamada, P. L. Baldeck and S. Parola, *Nanoscale*, 2014, **6**, 5138–5145.
9 J. H. Lee, K. J. Gibson, G. Chen and Y. Weizmann, *Nat. Commun.*, 2015, **6**, 7571.
10 G. W. Nyce, J. R. Hayes, A. V. Hamza and J. H. Satcher, *Chem. Mater.*, 2007, **19**, 344–346.
11 M. Kim, G. H. Jeong, K. Y. Lee, K. Kwon and S. W. Han, *J. Mater. Chem.*, 2008, **18**, 2208–2212.
12 K. Nishio and H. Masuda, *Angew. Chem., Int. Ed.*, 2011, **50**, 1603–1607.
13 N. Gandra, C. Portz and S. Singamaneni, *Adv. Mater.*, 2014, **26**, 424–429.
14 A. Wittstock, J. Biener and M. Baumer, *Phys. Chem. Chem. Phys.*, 2010, **12**, 12919–12930.
15 A. Jaiswal, L. M. Tian, S. Tadepalli, K. K. Liu, M. Fei, M. E. Farrell, P. M. Pellegrino and S. Singamaneni, *Small*, 2014, **10**, 4287–4292.
16 B. T. Su, Y. C. Tong, J. Bai, Z. Q. Lei, K. Wang, H. M. Mu and N. Doug, *Indian J. Chem., Sect. A: Inorg., Bio-inorg., Phys., Theor. Anal. Chem.*, 2007, **46**, 595–599.
17 B. Dong, B. L. He, C. L. Xu and H. L. Li, *Mater. Sci. Eng., B*, 2007, **143**, 7–13.
18 K. M. Molapo, P. M. Ndangili, R. F. Ajayi, G. Mbambisa, S. M. Mailu, N. Njomo, M. Masikini, P. Baker and E. I. Iwuoha, *Int. J. Electrochem. Sci.*, 2012, **7**, 11859–11875.
19 Z. Liu, L. Cheng, L. Zhang, Z. B. Yang, Z. Liu and J. X. Fang, *Biomaterials*, 2014, **35**, 4099–4107.
20 T. Lee, D. Bang, Y. Park, S. H. Kim, J. Choi, J. Park, D. Kim, E. Kim, J. S. Suh, Y. M. Huh and S. Haam, *Adv. Healthcare Mater.*, 2014, **3**, 1408–1414.
21 A. J. Coughlin, J. S. Ananta, N. F. Deng, I. V. Larina, P. Decuzzi and J. L. West, *Small*, 2014, **10**, 556–565.

22 W. I. Lin, C. Y. Lin, Y. S. Lin, S. H. Wu, Y. R. Huang, Y. Hung, C. Chang and C. Y. Mou, *J. Mater. Chem. B*, 2013, **1**, 639–645.
23 J. Lucon, S. Qazi, M. Uchida, G. J. Bedwell, B. LaFrance, P. E. Prevelige and T. Douglas, *Nat. Chem.*, 2012, **4**, 781–788.
24 T. Lee, D. Bang, Y. Park, Y. W. Chang, B. Kang, J. Kim, J. S. Suh, Y. M. Huh and S. Haam, *Eur. J. Inorg. Chem.*, 2015, 3740–3747, DOI: 10.1002/ejic.201500283.
25 S. E. Park, J. Lee, T. Lee, S. B. Bae, B. Kang, Y. M. Huh, S. W. Lee and S. Haam, *Int. J. Nanomed.*, 2015, **10**, 261–271.
26 D. Bang, T. Lee, J. Choi, Y. Park, E. Kim, Y. M. Huh and S. Haam, *Adv. Healthcare Mater.*, 2015, **4**, 255–263.
27 S. D. Perrault and W. C. Chan, *J. Am. Chem. Soc.*, 2009, **131**, 17042–17043.
28 T. Lee, E. K. Lim, J. Lee, B. Kang, J. Choi, H. S. Park, J. S. Suh, Y. M. Huh and S. Haam, *Nanoscale Res. Lett.*, 2013, **8**, 149.
29 H. B. Na, I. C. Song and T. Hyeon, *Adv. Mater.*, 2009, **21**, 2133–2148.
30 M. S. Ardestani, A. J. Arabzadeh, Z. Heidari, A. Hosseinzadeh, H. Ebrahimi, E. Hashemi, M. Mosayebnia, M. Shafiee-Alavidjeh, A. Alavi, M. H. Babaei, A. Rahmim, S. E. S. Ebrahimi and M. Amanlou, *J. Radioanal. Nucl. Chem.*, 2010, **283**, 447–455.
31 Z. L. Cheng, D. L. J. Thorek and A. Tsourkas, *Adv. Funct. Mater.*, 2009, **19**, 3753–3759.
32 J. S. Ananta, B. Godin, R. Sethi, L. Moriggi, X. W. Liu, R. E. Serda, R. Krishnamurthy, R. Muthupillai, R. D. Bolskar, L. Helm, M. Ferrari, L. J. Wilson and P. Decuzzi, *Nat. Nanotechnol.*, 2010, **5**, 815–821.
33 E. J. Werner, A. Datta, C. J. Jocher and K. N. Raymond, *Angew. Chem., Int. Ed.*, 2008, **47**, 8568–8580.
34 P. Caravan, *Chem. Soc. Rev.*, 2006, **35**, 512–523.